Magnetization Dynamics for Magnetic Object Interactions

SEUNG-WOOK KIM, Korea University
SUN YOUNG PARK, Korea University
JUNGHYUN HAN, Korea University

The goal of this paper is to simulate the interactions between magnetic objects in a physically correct way. The simulation scheme is based on magnetization dynamics, which describes the temporal change of magnetic moments. For magnetization dynamics, the Landau-Lifshitz-Gilbert equation is adopted, which is widely used in micromagnetics. Through effectively-designed novel models of magnets, it is extended into the macro scale so as to be combined with real-time rigid-body dynamics. The overall simulation is stable and enables us to implement mutual induction and remanence that have not been tackled by the state-of-the-art technique in magnet simulation. The proposed method can be applied to various fields including magnet experiments in the virtual world.

CCS Concepts: • **Computing methodologies** → **Physical simulation**;

Additional Key Words and Phrases: Magnetic fields and forces, magnetization, rigid body dynamics

ACM Reference Format:
Seung-wook Kim, Sun Young Park, and JungHyun Han. 2018. Magnetization Dynamics for Magnetic Object Interactions. *ACM Trans. Graph.* 37, 4, Article 121 (August 2018), 13 pages. https://doi.org/10.1145/3197517.3201402

1 INTRODUCTION

The last three decades have seen the prosperity of physics-based simulation in computer graphics. The results have been used in many areas including video games, visual effects in films, and education. A unique subfield of the physics-based simulation is focused on magnets. In the pioneering work of [Thomaszewski et al. 2008], the force and torque between magnetic objects were computed using the Maxwell's equations and integrated into rigid-body dynamics. Thanks to their efforts, magnetic simulation has recently begun to be adopted in education and art, as illustrated in Fig. 1. However, the potential demand of magnetic simulation requires the current techniques to advance one step further and address a few critical issues:

- **Magnetic mutual induction**: The magnetic induction of an object is determined by *all* magnetic objects in the environment. Fig. 2-(a) shows an example captured in a real-world experiment. Not only the bar magnet but also the iron ball in direct contact with it induces the second ball. The other balls are similarly induced by the balls preceding them and the bar magnet. Thus, we have a chain of induced magnets. Unfortunately, such mutual induction has not been tackled by the state-of-the-art techniques.
- **Magnetic remanence**: Many induced objects have a tendency of preserving magnetization for a certain period of time. Fig. 2-(b) shows a well-known example of first magnetizing a metallic material and then using its remanence to magnetize other objects. There has been no attempt to implement this phenomenon.
- **Simulation stability**: A magnetic object exposed to a magnetic field is accelerated by a magnetic force. In general, the closer the magnetic objects are to each other, the more induced they become, and thus the magnetic forces that they produce become stronger. This often causes the magnetic objects to interpenetrate each other and produce much stronger magnetic forces, which eventually make the simulation unstable. In order to resolve this problem, a smaller time step size can be used in the rigid-body simulation. However, this is not appropriate for real-time simulation.

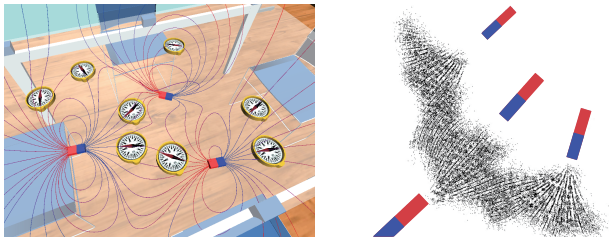

(a) (b)

Fig. 1. The state of the art in magnet simulation: (a) Magnetic field lines and compasses [Park et al. 2016]. (b) Iron filing art [Yoon et al. 2014].

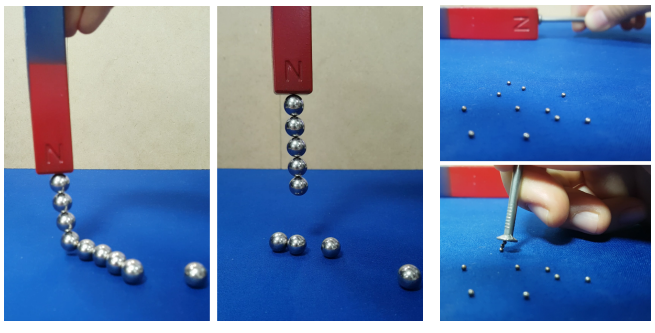

(a) (b)

Fig. 2. Indispensable components of virtual magnet experiments: (a) Mutual induction. (b) Remanence.

Authors' addresses: Seung-wook Kim, Korea University, wook0249@korea.ac.kr; Sun Young Park, Korea University, iamsun0720@korea.ac.kr; JungHyun Han, Korea University, jhan@korea.ac.kr.

0730-0301/2018/8-ART121 $15.00
https://doi.org/10.1145/3197517.3201402

While we were building a magnetic simulation system, we encountered various difficulties and realized the critical issues listed above. Searching for solutions, we have focused on the core subjects in magnetics, which have been proven to be physically correct. The first step was to adopt the Landau-Lifshitz-Gilbert (LLG) equation, which describes *magnetization dynamics* in micromagnetics. It asserts that magnetization of an object does not increase above a certain point but is saturated. This property of saturated magnetization helps prevent the magnetic forces from becoming excessively large. For the LLG equation to work at the macro scale, we have designed novel magnet models and developed efficient algorithms which work on them.

The LLG equation is proven to have a special structure, which guarantees non-divergence of the magnetic energy. Together with the intrinsic property of saturated magnetization, the structure ensures the stable simulation of rigid bodies. This is a remarkable strength of the LLG equation because divergence is the main barrier to mutual induction, as pointed out by [Thomaszewski et al. 2008]. Our algorithms process the permanent magnets and the objects to be induced by them in a uniform fashion, and the LLG equation enables successful implementation of mutual induction.

If magnetization were computed from scratch for every step of the rigid-body simulation, the phenomenon of magnetic remanence could not be implemented. Based on the novel models of magnets, our algorithms compute the change of magnetization over time, making it possible to implement magnetic remanence.

2 RELATED WORK

A material that can be strongly induced by magnetic fields is called a ferromagnet. Ferromagnetism has been extensively studied in computational and applied physics, material science, electrical engineering, etc. According to the spatial scales, it is classified into macroscopic and microscopic categories. The macro-scale ferromagnetism uses the so-called phenomenological constitutive relations, which describe the evolution of magnetization [Kruzík and Prohl 2006]. Well-known is the linear constitutive relation, which asserts that magnetization of a magnetic object is linearly proportional to the magnetic field applied to it [Aharoni 2000]. Due to its excessive approximation, however, this relation often fails to fully account for the principles of ferromagnetism.

A lot of works on the micro-scale ferromagnetism use the LLG equation for the time evolution of magnetization in order to obtain the magnetization in equilibrium through integration. Such a magnetization dynamics is widely studied especially in the field of magnetic recording. A good survey on the LLG equation can be found in [Lakshmanan 2011].

The work of [Thomaszewski et al. 2008] has been the only one in the computer graphics area for magnetic interaction integrated with rigid-body simulation. Based on the linear constitutive relation in magnetostatic environments, magnetization was determined by the magnetic fields generated by permanent magnets to produce magnetic forces and torques. The proposed method did not address the issues discussed in Section 1.

In the domain of magnetic simulation of non-rigid elements, [Ishikawa et al. 2013] simulated magnetic fluids using the Smoothed Particle Hydrodynamics (SPH) method [Müller et al. 2003]. They expressed spikes at the surface of the magnetic fluid using an energy minimization scheme. There have been a few notable efforts in the context of magnetostatic visualization: Particles were used to express magnetic field lines [Klein and Ertl 2004], magnetic fields were visualized revealing the topology of magnetic flux [Bachthaler et al. 2012], magnetic field lines were visualized for virtual science classes [Park et al. 2016], and iron filings were graphically generated in an artistic approach [Yoon et al. 2014].

Magnets have been used in animations such as Robots, Toy Story 3, and Despicable Me 2, and also in visual effects for Spider-Man 2, Transformers: Age of Extinction, Under the Dome, etc. Interestingly, Robots presented the remanence effect, which was apparently implemented by hand.

3 MICROMAGNETICS

A magnet produces a *magnetic field*. If a material is strongly induced along the direction of the magnetic field, it is named a *ferromagnet*. In contrast, a *paramagnet* is weakly induced. A ferromagnet is called *hard* if it tends to preserve its magnetization. Otherwise, it is called *soft*. The examples of hard ferromagnet are alnico and ferrite, those of soft ferromagnet are iron and nickel, and those of paramagnet are aluminum and magnesium.

A *permanent magnet* is manufactured from a hard ferromagnet through a specialized process under a strong magnetic field. This paper focuses on interactions between permanent magnets and soft ferromagnets. The soft ferromagnets are induced by the permanent magnets, and they all undergo rigid-body motions.

3.1 Magnetic Moment and Magnetization

The vector quantities that cause the rigid-body motion of a magnetic object are the *magnetic dipole moments* or simply *magnetic moments*. When an object that has electric properties (such as electron and the Earth) moves or rotates, it produces an electric current which creates a magnetic moment. Given a distribution of the electric current density $\mathbf{J}$, the magnetic moment $\boldsymbol{\mu}$ is defined as follows [Jackson 1999]:

$$\boldsymbol{\mu} = \frac{1}{2}\int_V (\mathbf{x}-\mathbf{p})\times\mathbf{J}(\mathbf{x}-\mathbf{p})\,d^3x \tag{1}$$

where $\boldsymbol{\mu}$ is defined at $\mathbf{p}$ that represents an arbitrary point in volume V. The magnetic moment density, i.e., the magnetic moment per unit volume, is named *magnetization*. It is also a vector quantity and is denoted as $\mathbf{M}$.

The key element that distinguishes between hard and soft ferromagnets is the *magnetic anisotropy*, which refers to the directional dependence of a material's magnetic properties [Aharoni 2000]. A hard ferromagnet has strong magnetic anisotropy regardless of its shape whereas a soft ferromagnet has no or weak magnetic anisotropy. An *easy axis* is referred to as an energetically favorable direction of spontaneous magnetization. A ferromagnet with magnetic anisotropy has a set of easy axes, and it tends to align its magnetization along an easy axis.

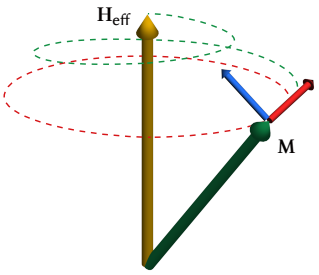

Fig. 3. $\mathbf{M}$ moves precessionally (along the red arrow) around $\mathbf{H}_{\text{eff}}$, and its trajectory is a circle (in dotted red). When the damping motion (along the blue arrow) is added, the combined motion is a spiral (in dotted green) centered about $\mathbf{H}_{\text{eff}}$.

3.2 Effective Magnetic Field

Consider a point $\mathbf{q}$ in space. The *effective magnetic field*, $\mathbf{H}_{\text{eff}}$, at $\mathbf{q}$ is defined as the sum of four components [Nakatani et al. 1989]:

$$\mathbf{H}_{\text{eff}} = \mathbf{H}_{\text{E}} + \mathbf{H}_{\text{D}} + \mathbf{H}_{\text{X}} + \mathbf{H}_{\text{K}} \tag{2}$$

where $\mathbf{H}_{\text{E}}$ is the external field such as the Earth's, $\mathbf{H}_{\text{D}}$ is the demagnetizing field, $\mathbf{H}_{\text{X}}$ is the exchange field, and $\mathbf{H}_{\text{K}}$ is the magnetocrystalline anisotropy field.

$\mathbf{H}_{\text{D}}$ describes the contributions from all magnetic moments in the environment. Given n magnetic moments, each denoted as $\boldsymbol{\mu}_i$, $\mathbf{H}_{\text{D}}$ at $\mathbf{q}$ is defined as follows [Jackson 1999]:

$$\mathbf{H}_{\text{D}} = \frac{1}{4\pi}\sum_{i=1}^{n}\left(\frac{3\mathbf{r}_i\left(\mathbf{r}_i\cdot\boldsymbol{\mu}_i\right)}{\|\mathbf{r}_i\|^5} - \frac{\boldsymbol{\mu}_i}{\|\mathbf{r}_i\|^3}\right) \tag{3}$$

where $\mathbf{r}_i$ is the vector from the position of $\boldsymbol{\mu}_i$ to $\mathbf{q}$.

The exchange field, $\mathbf{H}_{\text{X}}$, is generated by the quantum mechanical effect. It is related to the Laplacian of the magnetic moment's axial components and plays an important role in micromagnetics. In contrast, the distances between magnetic moments in the macro-scale model are usually too large for $\mathbf{H}_{\text{X}}$ to bring about nonnegligible effects. Therefore, we ignore $\mathbf{H}_{\text{X}}$ in our macro-scale simulation.

The *magnetocrystalline anisotropy* determines its own easy axes in a ferromagnet. If the direction of magnetization $\mathbf{M}$ is different from all easy axes, $\mathbf{H}_{\text{K}}$ is generated. It drives $\mathbf{M}$ to get aligned with an easy axis. Section 3.3 will give a detailed discussion of how $\mathbf{H}_{\text{K}}$ works.

3.3 Landau-Lifshitz-Gilbert Equation

Landau-Lifshitz-Gilbert (LLG) equation [Gilbert 1955] describes the *magnetization dynamics*, i.e., the dynamics of magnetic moments. It is widely used in micromagnetics to update the magnetic moments in an extremely large number of infinitesimally small magnetic domains. In the LLG equation, the change over time of magnetization, $\mathbf{M}$, exposed to $\mathbf{H}_{\text{eff}}$ is described as follows [Lakshmanan 2011]:

$$\frac{d\mathbf{M}}{dt} = -\gamma\left(\mathbf{M}\times\mathbf{H}_{\text{eff}} - \eta\left(\mathbf{M}\times\frac{d\mathbf{M}}{dt}\right)\right) \tag{4}$$

where γ is the gyromagnetic ratio and η is the material-specific damping constant. The first and second terms inside of the outer parenthesis in Equation (4) correspond respectively to the *precessional motion* and *damping motion* of $\mathbf{M}$ illustrated in Fig. 3. $\mathbf{M}$ will be in equilibrium either if it is aligned with $\mathbf{H}_{\text{eff}}$ or if $\mathbf{H}_{\text{eff}} = \mathbf{0}$.

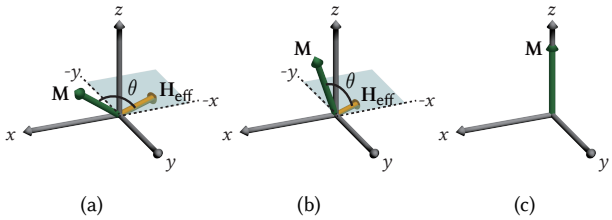

Fig. 4. $\mathbf{H}_{\text{eff}}$ and $\mathbf{M}$: (a) Initial configuration. (b) $\mathbf{M}$ and $\mathbf{H}_{\text{eff}}$ are updated. (c) Final configuration.

Let us dot-multiply both sides of Equation (4) with $\mathbf{M}$:

$$\frac{d\mathbf{M}}{dt}\cdot\mathbf{M} = -\gamma\left(\mathbf{M}\times\mathbf{H}_{\text{eff}} - \eta\left(\mathbf{M}\times\frac{d\mathbf{M}}{dt}\right)\right)\cdot\mathbf{M} \tag{5}$$

Obviously the right-hand side becomes zero, and therefore $\frac{d\mathbf{M}}{dt}\cdot\mathbf{M} = 0$, which implies that the magnitude of $\mathbf{M}$ remains constant over time.

Using the above observation, let us now present how $\mathbf{H}_{\text{eff}}$ updates $\mathbf{M}$. For a uniaxially anisotropic ferromagnet, $\mathbf{H}_{\text{K}}$ is defined to be orthogonal to its easy axis [Nakatani et al. 1989]. If the easy axis is the z-axis, for example, $\mathbf{H}_{\text{K}}$ is defined in the plane spanned by the x- and y-axes. When $\mathbf{M} = \left(M_x, M_y, M_z\right)^T$, $\mathbf{H}_{\text{K}}$ is defined as follows:

$$\mathbf{H}_{\text{K}} = -\frac{2K_u}{M_s}\begin{pmatrix} M_x \\ M_y \\ 0 \end{pmatrix} \tag{6}$$

where K_u is the anisotropy constant and M_s denotes $\|\mathbf{M}\|$.

Assume that $\mathbf{H}_{\text{K}}$ is the dominant component of $\mathbf{H}_{\text{eff}}$, i.e., $\mathbf{H}_{\text{eff}} \simeq \mathbf{H}_{\text{K}}$. Without loss of generality, $\mathbf{H}_{\text{eff}}$ can then be considered to lie in the xy-plane, as illustrated in Fig. 4-(a). Obviously, the angle, θ, between $\mathbf{M}$ and $\mathbf{H}_{\text{eff}}$ is obtuse.

Due to the damping motion presented in Equation (4) and Fig. 3, θ will decrease. It implies that M_z will increase whereas $\sqrt{{M_x}^2 + {M_y}^2}$ will decrease because the magnitude of $\mathbf{M}$ remains constant. Consequently, $\mathbf{M}$ gets closer to the z-axis. See Fig. 4-(b).

On the other hand, changed M_x and M_y will update $\mathbf{H}_{\text{K}}$, which will then update $\mathbf{H}_{\text{eff}}$. Consequently, the magnitude of $\mathbf{H}_{\text{eff}}$ will decrease, being confined in the xy-plane. This is also illustrated in Fig. 4-(b).

When these steps are repeated, $\mathbf{H}_{\text{eff}}$ will keep decreasing to zero, and $\mathbf{M}$ will be aligned with the z-axis, which is the easy axis. See Fig. 4-(c).

3.4 Numerical Integration for Magnetization Dynamics

Let us normalize $\mathbf{M}$ and denote it as $\mathbf{m}$, i.e., $\mathbf{m} = \mathbf{M}/M_s$, where $M_s = \|\mathbf{M}\|$. The LLG equation presented in Equation (4) then becomes

$$\frac{d\mathbf{m}}{dt} = -\gamma\left(\mathbf{m}\times\mathbf{H}_{\text{eff}} - \eta M_s\left(\mathbf{m}\times\frac{d\mathbf{m}}{dt}\right)\right) \tag{7}$$

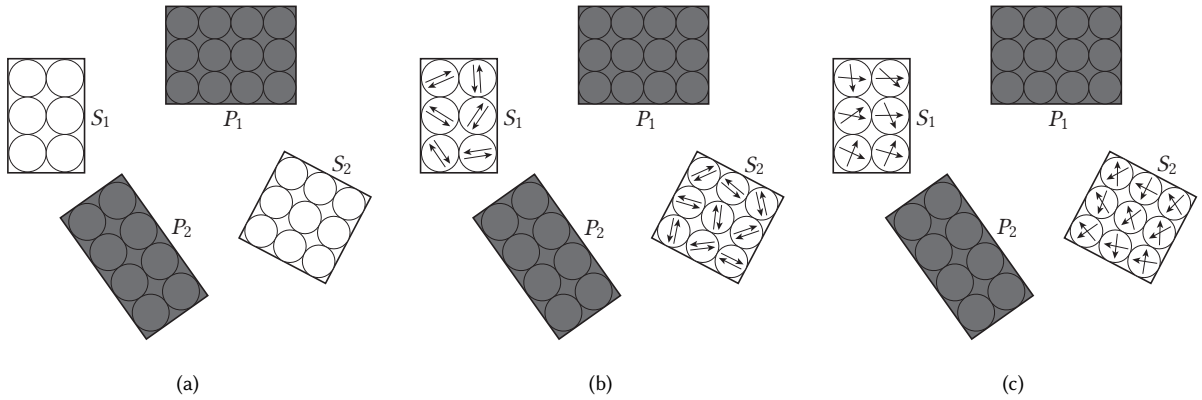

Fig. 5. Permanent magnets (shaded) and soft ferromagnets: (a) Every magnetic object is decomposed into spherical cells. (b) In a soft ferromagnet, multiple instances of the normalized magnetic moment are assigned to a cell. (c) The magnetic moments are rotated through simulation.

As proposed by [Brown 1979], Equation (7) can be transformed into a closed form:

$$\frac{d\mathbf{m}}{dt} = -\frac{\gamma}{1+\alpha^2}(\mathbf{m}\times\boldsymbol{\mathcal{H}}) \tag{8}$$

where α and $\boldsymbol{\mathcal{H}}$ are defined as follows:

$$\begin{aligned}\alpha &= \gamma\eta M_s\\ \boldsymbol{\mathcal{H}} &= \mathbf{H}_{\text{eff}} + \alpha(\mathbf{m}\times\mathbf{H}_{\text{eff}})\end{aligned} \tag{9}$$

Using Equation (8), the rotation of the magnetic moment can be simulated in a numerical way. For numerical integration, consider the mid-point method [Serpico et al. 2001]. For the $\left(i+\frac{1}{2}\right)$-th step of the simulation, the first order approximations of $\mathbf{m}$ and $\frac{d\mathbf{m}}{dt}$ are defined as follows:

$$\mathbf{m}^{i+\frac{1}{2}} = \frac{\mathbf{m}^{i+1}+\mathbf{m}^{i}}{2} \tag{10}$$

$$\left(\frac{d\mathbf{m}}{dt}\right)^{i+\frac{1}{2}} = \frac{\mathbf{m}^{i+1}-\mathbf{m}^{i}}{\Delta t} \tag{11}$$

Equations (10) and (11) are inserted into Equation (8):

$$\mathbf{m}^{i+1}-\mathbf{m}^{i} = -\frac{\gamma\Delta t}{2\left(1+\alpha^2\right)}\left(\left(\mathbf{m}^{i+1}+\mathbf{m}^{i}\right)\times\boldsymbol{\mathcal{H}}^{i+\frac{1}{2}}\right) \tag{12}$$

where the first order approximation of $\boldsymbol{\mathcal{H}}^{i+\frac{1}{2}}$ is defined as follows:

$$\begin{aligned}\boldsymbol{\mathcal{H}}^{i+\frac{1}{2}} &= \frac{\boldsymbol{\mathcal{H}}^{i+1}+\boldsymbol{\mathcal{H}}^{i}}{2}\\ &= \frac{\left(2\boldsymbol{\mathcal{H}}^{i}-\boldsymbol{\mathcal{H}}^{i-1}\right)+\boldsymbol{\mathcal{H}}^{i}}{2}\\ &= \frac{3}{2}\boldsymbol{\mathcal{H}}^{i}-\frac{1}{2}\boldsymbol{\mathcal{H}}^{i-1}\end{aligned} \tag{13}$$

The mid-point method works when $i>0$. When $i=0$, the second-order Runge-Kutta integration is used. It is straightforward to show that the magnitude of $\mathbf{m}$ is preserved during the integration. If we dot-multiply both sides of Equation (12) with $(\mathbf{m}^{i+1}+\mathbf{m}^{i})$, we obtain the following:

$$\left(\mathbf{m}^{i+1}-\mathbf{m}^{i}\right)\cdot\left(\mathbf{m}^{i+1}+\mathbf{m}^{i}\right) = 0 \tag{14}$$

This leads to $\|\mathbf{m}^{i}\| = \|\mathbf{m}^{i+1}\|$, i.e. the magnitude of $\mathbf{m}$ is unconditionally preserved.

4 MACRO-SCALE MAGNETIZATION SIMULATION

The magnetics introduced in Section 3 works at the micro scale. This section presents how to extend it into the macro scale so as to be combined with real-time rigid-body dynamics of magnetic objects.

4.1 Cell Decomposition and Magnetic Moments

We decompose each magnetic object into a set of uniform spherical cells [Thomaszewski et al. 2008]. Fig. 5-(a) shows an example with two permanent magnets (P_1 and P_2) and two soft ferromagnets (S_1 and S_2).

First of all, consider a permanent magnet. Let V denote its cell's volume. Assuming that a cell is uniformly magnetized across V, its net magnetic moment, $\boldsymbol{\mu}$, defined at the cell's center is expressed as $\mathbf{M}V$, where $\mathbf{M}$ denotes the magnetization of the cell. $\mathbf{M}$ is established when the permanent magnet is manufactured. It is fixed, and therefore every cell of a permanent magnet is assigned the same $\boldsymbol{\mu}$.

Similarly, $\boldsymbol{\mu}$ of a soft ferromagnet's cell is defined at the cell's center. In contrast to permanent magnets, however, $\boldsymbol{\mu}$ in a soft ferromagnet is dynamically aligned along the effective magnetic field, and therefore $\boldsymbol{\mu}$ may be different across the cells. We will present how to compute $\boldsymbol{\mu}$ of each cell, equivalently its magnetization $\mathbf{M}$.

4.2 Effective Magnetic Field at the Macro Scale

Magnetic simulation at the macro scale requires iterations of updating the effective magnetic field $\mathbf{H}_{\text{eff}}$ and magnetic moment $\boldsymbol{\mu}$ (or magnetization $\mathbf{M}$) for each cell. Consider the components of $\mathbf{H}_{\text{eff}}$ presented in Equation (2). Obviously, $\mathbf{H}_{\text{E}}$ remains unchanged between the micro and macro scales. In contrast, $\mathbf{H}_{\text{D}}$ and $\mathbf{H}_{\text{K}}$ should be redefined. ($\mathbf{H}_{\text{X}}$ is ignored in the macro-scale simulation, as discussed in Section 3.2.)

In Equation (3), $\mathbf{H}_{\text{D}}$ is specified in terms of microscopic magnetic moments, each defined in a nanometer-scale volume. In our macro-scale model, a millimeter-scale cell encompasses many such

microscopic magnetic moments. In terms of cells, $\mathbf{H}_{\mathrm{D}}$ is decomposed into what we denote as $\mathbf{H}_{\mathrm{exo\_D}}$ and $\mathbf{H}_{\mathrm{endo\_D}}$. $\mathbf{H}_{\mathrm{exo\_D}}$ is generated by other cells in the environment. $\mathbf{H}_{\mathrm{endo\_D}}$ accounts for the interactions between the microscopic magnetic moments "in a cell."

Let C_{ij} represent the i-th magnetic object's j-th cell, and $\boldsymbol{\mu}_{ij}$ represents the magnetic moment of C_{ij}. Then, $\mathbf{H}_{\mathrm{D}}$ in Equation (3) is modified to define $\mathbf{H}_{\mathrm{exo\_D}}$:

$$\mathbf{H}_{\mathrm{exo\_D}} = \frac{1}{4\pi}\sum_i\sum_j\left(\frac{3\mathbf{r}_{ij}\left(\mathbf{r}_{ij}\cdot\boldsymbol{\mu}_{ij}\right)}{\|\mathbf{r}_{ij}\|^5} - \frac{\boldsymbol{\mu}_{ij}}{\|\mathbf{r}_{ij}\|^3}\right) \tag{15}$$

where $\mathbf{r}_{ij}$ is the vector from the center of C_{ij} to that of the current cell.

The magnetic field exerted on a cell is generated by *all* magnetic objects in the environment, which include not only the permanent magnets but also the induced magnets. Consider the example in Fig. 5-(a). Once S_1 is magnetized by P_1 and P_2, S_1 applies a magnetic field to S_2 together with P_1 and P_2. Then, the magnetization of S_2 is updated, and in return S_2 applies a magnetic field to S_1. This is *mutual induction*. It is important to note that $\boldsymbol{\mu}_{ij}$ in Equation (15) may come from an induced magnet as well as a permanent magnet. Equation (15) processes both permanent and induced magnets uniformly to support mutual induction.

In general, calculation of $\mathbf{H}_{\mathrm{endo\_D}}$ requires us to consider the boundary conditions for the cell's shape, which is usually costly and bothersome. Fortunately, an analytic solution is available for the spherical cell. Let $\mathbf{M}$ denote the magnetization of the cell determined at the "current iteration" of our time-stepping scheme. Then, $\mathbf{H}_{\mathrm{endo\_D}}$ is simply defined in terms of $\mathbf{M}$ [Jackson 1999]:

$$\mathbf{H}_{\mathrm{endo\_D}} = -\gamma_D\mathbf{M} \tag{16}$$

where γ_D is called the demagnetizing factor. For a uniformly magnetized sphere, γ_D is proven to be $1/3$ [Osborn 1945].

$\mathbf{H}_{\mathrm{K}}$ at the macro scale is defined in the same manner as at the micro scale. Suppose that $\boldsymbol{\mu} = (\mu_x, \mu_y, \mu_z)^T$. Given a uniaxially anisotropic ferromagnet, the easy axis of which is the z-axis, its $\mathbf{H}_{\mathrm{K}}$ is defined as follows:

$$\mathbf{H}_{\mathrm{K}} = -\frac{2K_u}{M_s V}\begin{pmatrix}\mu_x\\ \mu_y\\ 0\end{pmatrix} \tag{17}$$

Equation (17) just rephrases Equation (6) using the fact that $\boldsymbol{\mu} = \mathbf{M}V$.

In summary, the effective magnetic field at the macro scale is defined as follows:

$$\mathbf{H}_{\mathrm{eff}} = \mathbf{H}_{\mathrm{E}} + \mathbf{H}_{\mathrm{exo\_D}} + \mathbf{H}_{\mathrm{endo\_D}} + \mathbf{H}_{\mathrm{K}} \tag{18}$$

4.3 Saturated Magnetization

In Equation (18), $\mathbf{H}_{\mathrm{E}}$ and $\mathbf{H}_{\mathrm{exo\_D}}$ are caused by the magnetic moments located outside of the cell. $\mathbf{H}_{\mathrm{E}} + \mathbf{H}_{\mathrm{exo\_D}}$ is called the *applied* magnetic field and denoted as $\mathbf{H}_{\mathrm{A}}$. When $\mathbf{H}_{\mathrm{A}}$ is weak, $\mathbf{M}$ and $\mathbf{H}_{\mathrm{A}}$ at the macro scale are related as follows [Aharoni 2000]:

$$\mathbf{M} = \chi\mathbf{H}_{\mathrm{A}} \tag{19}$$

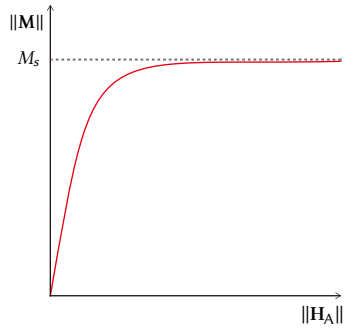

Fig. 6. $\mathbf{M}$ varies linearly with $\mathbf{H}_{\mathrm{A}}$ only when $\mathbf{H}_{\mathrm{A}}$ is weak. As the strength of $\mathbf{H}_{\mathrm{A}}$ increases, the derivative of $\mathbf{M}$ decreases, eventually leading to the saturated magnetization.

χ denotes the *susceptibility* of a material. It is determined by the material's *intrinsic susceptibility*, χ_i, and its shape [Cao et al. 2014]:

$$\chi = \frac{\chi_i}{1 + \gamma_D\chi_i} \tag{20}$$

where γ_D is determined by the shape of the magnetic object and is $1/3$ for a spherical object. In general, χ_i of a ferromagnet is fairly big, and therefore χ is approximated to $1/\gamma_D$.

In the real-world measurements of magnetization, it has been found that the magnitude of $\mathbf{M}$ does not increase above a material-specific value but is *saturated* [Grössinger 1981]. If we ignore this feature, $\mathbf{M}$ can be excessively large as $\mathbf{H}_{\mathrm{A}}$ increases, resulting in an unstable rigid-body simulation. In principle, $\mathbf{M}$ and $\mathbf{H}_{\mathrm{A}}$ are related as follows [Abbott et al. 2007]:

$$\mathbf{M} = \begin{cases}\dfrac{1}{\gamma_D}\mathbf{H}_{\mathrm{A}} & \text{if } \|\mathbf{H}_{\mathrm{A}}\| < H_s\\ M_s\dfrac{\mathbf{H}_{\mathrm{A}}}{\|\mathbf{H}_{\mathrm{A}}\|} & \text{otherwise}\end{cases} \tag{21}$$

where H_s represents the minimum strength of $\mathbf{H}_{\mathrm{A}}$ to make the magnetization saturated, and M_s represents the magnitude of the 'saturated' magnetization. Note that the definition of M_s is different between micro and macro scales.

Fig. 6 depicts the general magnetization curve [Grössinger 1981], which is determined by various material-specific factors (including the inhomogeneities and anisotropy) of a ferromagnet as well as Equation (21). Section 3.3 showed that, even though the direction of $\mathbf{M}$ changes, its magnitude remains constant over time. It is the microscopic view, i.e., it is for a magnetic moment defined in a nanometer-scale volume. In contrast, Fig. 6 shows the macroscopic view: The magnitude of $\mathbf{M}$ is not constant. Consider a cell, where many microscopic moments reside. If their vector sum is zero, for example, the cell's $\mathbf{M}$ becomes zero.

4.4 Magnet Modeling and Simulation

A soft ferromagnet is decomposed into cells. In [Thomaszewski et al. 2008], the magnetic moment of a cell was analytically computed from scratch at each step of rigid-body simulation. In contrast, we first assign multiple instances of the 'normalized' magnetic moment, each denoted as $\mathbf{m}_i$, to a cell and simulate the dynamics of $\mathbf{m}_i$ using

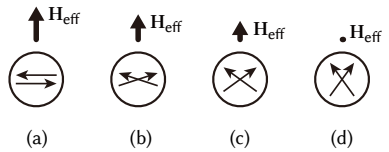

Fig. 7. Iterations of updating $\mathbf{H}_{\text{eff}}$, $\mathbf{m}_1$, and $\mathbf{m}_2$.

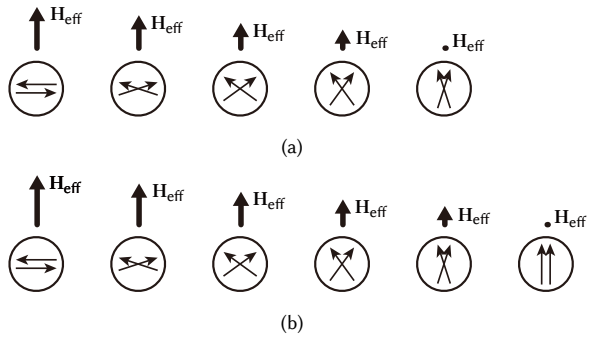

Fig. 8. Iterations of updating $\mathbf{H}_{\text{eff}}$, $\mathbf{m}_1$, and $\mathbf{m}_2$: (a) The initial vector for $\mathbf{H}_{\text{eff}}$ is increased. (b) $\mathbf{H}_{\text{eff}}$ is further increased.

the LLG equation. Note that $\mathbf{m}_i$ corresponds to the normalized magnetization, $\mathbf{m}$, presented in Section 3.4.

Why not a single magnetic moment in a cell? The direction of the magnetic moment may change but its magnitude remains constant, as discussed in Section 3.3, and consequently the magnetization curve presented in Fig. 6 cannot be implemented in a cell.

Fig. 5-(b) shows the simplest implementation of assigning two normalized magnetic moments to a cell. (Their initial directions are randomly chosen across the cells. Our experimental results show that the initial directions make an insignificant impact on the simulation results.) Let us denote the magnetic moments by $\mathbf{m}_1$ and $\mathbf{m}_2$. The directions of $\mathbf{m}_1$ and $\mathbf{m}_2$ are initialized to be opposite, i.e., $\mathbf{m}_1 = -\mathbf{m}_2$. As $\mathbf{M} = \frac{1}{2}(\mathbf{m}_1 + \mathbf{m}_2)M_s$, the initial orientations of $\mathbf{m}_1$ and $\mathbf{m}_2$ make $\mathbf{M}$ zero, implying that the object is not magnetized. For each iteration of magnetic simulation, the directions of $\mathbf{m}_1$ and $\mathbf{m}_2$ will be updated by $\mathbf{H}_{\text{eff}}$, as depicted in Fig. 5-(c).

For the sake of simplicity, consider a single-cell isotropic ($\mathbf{H}_{\text{K}} = \mathbf{0}$) object exposed to $\mathbf{H}_{\text{E}}$. Assume that there is no other magnetic object in the environment. Then, $\mathbf{H}_{\text{exo\_D}} = \mathbf{0}$ and $\mathbf{H}_{\text{A}} = \mathbf{H}_{\text{E}}$. Initially, $\mathbf{H}_{\text{eff}} = \mathbf{H}_{\text{E}}$. Shown in Fig. 7-(a) are initial $\mathbf{H}_{\text{eff}}$, $\mathbf{m}_1$, and $\mathbf{m}_2$. Fig. 7-(b) shows $\mathbf{m}_1$ and $\mathbf{m}_2$ updated by $\mathbf{H}_{\text{eff}}$. They are more aligned with $\mathbf{H}_{\text{eff}}$. Then, $\mathbf{M}$ is no longer zero. It generates $\mathbf{H}_{\text{endo\_D}}$, which is defined to be $-\frac{1}{3}\mathbf{M}$, as presented in Section 4.2. $\mathbf{H}_{\text{endo\_D}}$ is added to $\mathbf{H}_{\text{eff}}$, which is then decreased, as illustrated in Fig. 7-(b).

Fig. 7-(c) shows the next iteration's result. In Fig. 7-(d), $\mathbf{H}_{\text{eff}}$ becomes zero, leading to equilibrium. The simulation is terminated, and $\mathbf{M}$ is no longer updated. Observe that, in Fig. 7-(d), $\mathbf{m}_1$ and $\mathbf{m}_2$ are not of the same direction. $\mathbf{M}$ does not reach the maximum magnitude, M_s.

Now suppose that $\mathbf{H}_{\text{E}}$ is increased. Fig. 8-(a) shows how $\mathbf{H}_{\text{eff}}$ and the magnetic moments change. Observe that, when the simulation

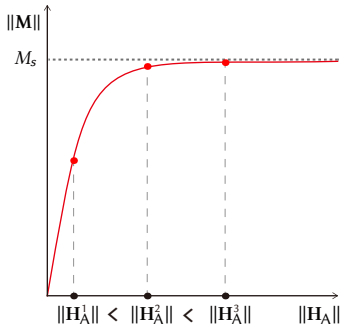

Fig. 9. Three instances of $\mathbf{H}_{\text{A}}$ represent the cases presented in Fig. 7, Fig. 8-(a), and Fig. 8-(b) in order.

is completed, $\mathbf{M}$ in Fig. 8-(a) is larger than that in Fig. 7. Fig. 8-(b) shows the case when $\mathbf{H}_{\text{E}}$ is further increased. As the final directions of $\mathbf{m}_1$ and $\mathbf{m}_2$ are the same, $\mathbf{M}$ reaches the maximum magnitude, M_s, i.e., the state of saturated magnetization. Fig. 9 plots the three examples on the magnetization curve.

Note that simulation with the LLG equation requires pre-existence of a magnetic moment such that its rotation is determined through integration. Assigning multiple magnetic moments to a cell is the key feature of our magnet modeling. By doing so, zero-magnetization cell can be neatly defined, and both pre-saturation and saturation stages presented in Fig. 9 can be implemented in a cell.

In Fig. 7 and Fig. 8, the magnetic moments initialized in a cell are illustrated as if they were separated, just for visualization purposes. In reality, they are located at the cell's center, i.e. they share the same position, and consequently they are updated by the same $\mathbf{H}_{\text{eff}}$.

Let us now refine the components of $\mathbf{H}_{\text{eff}}$ for our magnet model. Suppose that we have n magnetic moments in a cell. After a step of magnetic simulation, the resulting magnetization, $\mathbf{M}$, is defined as

$$\left(\frac{1}{n}\sum_{i=1}^{n}\mathbf{m}_i\right)M_s \tag{22}$$

Then, $\mathbf{H}_{\text{exo\_D}}$ and $\mathbf{H}_{\text{endo\_D}}$ are accordingly defined. By replacing $\boldsymbol{\mu}_{ij}$ with $\mathbf{M}_{ij}V_i$ in Equation (15), $\mathbf{H}_{\text{exo\_D}}$ is obtained. ($\mathbf{M}_{ij}$ represents the magnetization of the i-th magnetic object's j-th cell, and V_i represents the cell's volume of the i-th magnetic object.) By inserting $\mathbf{M}$ into Equation (16), $\mathbf{H}_{\text{endo\_D}}$ is obtained:

$$\mathbf{H}_{\text{endo\_D}} = -\gamma_D\mathbf{M} = -\gamma_D\left(\frac{1}{n}\sum_{i=1}^{n}\mathbf{m}_i\right)M_s \tag{23}$$

Note that, in Equation (17), M_sV represents the magnitude of a magnetic moment and therefore division by M_sV is equivalent to taking the x- and y-coordinates of the *normalized* magnetic moment. In our magnet model, $\mathbf{m}_i$ is a normalized magnetic moment per se. As $\mathbf{m}_i = (m_{i_x}, m_{i_y}, m_{i_z})^T$, Equation (17) can be rephrased as follows:

$$\mathbf{H}_{\text{K},i} = -2K_u\begin{pmatrix} m_{i_x} \\ m_{i_y} \\ 0 \end{pmatrix} \tag{24}$$

Algorithm 1 Magnetic simulation

```
1: iter := 0
2: compute the demagnetizing tensor, D_ij
3: while error > ε and iter < maxIter do
4:     for each magnetic moment m do
5:         compute H_eff
6:         integrate m over the time step using Equation (12)
7:     compute error
8:     iter := iter + 1
```

Equation (24) applies independently to every magnetic moment in a cell.

Returning to Fig. 8-(b), suppose that, after $\mathbf{M}$ in the cell is saturated, $\mathbf{H}_{\text{E}}$ becomes weaker. Then, $\mathbf{M}$ should be accordingly decreased. However, the magnetic moments with the same direction cannot be made different even though they are updated by $\mathbf{H}_{\text{eff}}$. Consequently, $\mathbf{M}$ remains saturated.

This problem could be handled by restoring the magnetic moment to its initial state. Unfortunately, this simple solution disables the remanence effects since the history of the magnetic moment is ignored. Our solution is to perturb the magnetic moment slightly, i.e., $\mathbf{H}_{\text{eff}}$ is augmented with what we call *noise field*. It is a feeble magnetic field randomly determined per magnetic moment. In the current implementation, its magnitude is 10^{-6} times $\mathbf{H}_{\text{eff}}$'s. A magnetic moment parallel or antiparallel to $\mathbf{H}_{\text{eff}}$ would not be rotated without a noise field.

Understand that each magnetic moment in a cell is associated with its own $\mathbf{H}_{\text{K}}$ and the noise field whereas $\mathbf{H}_{\text{E}}$, $\mathbf{H}_{\text{exo\_D}}$, and $\mathbf{H}_{\text{endo\_D}}$ are shared by multiple magnetic moments.

4.5 Magnetic Simulation + Rigid-body Simulation

In our magnetic simulation, the most time-consuming part is computing $\mathbf{H}_{\text{eff}}$. Especially, most of the time is consumed by $\mathbf{H}_{\text{exo\_D}}$ computation. Given N magnetic moments, its time complexity is $O(N^2)$. Fortunately, Equation (15) can be rephrased as follows:

$$\begin{aligned}\mathbf{H}_{\text{exo\_D}} &= \frac{1}{4\pi}\sum_i\sum_j\left(\frac{3\mathbf{r}_{ij}\left(\mathbf{r}_{ij}\cdot\boldsymbol{\mu}_{ij}\right)}{\|\mathbf{r}_{ij}\|^5}-\frac{\boldsymbol{\mu}_{ij}}{\|\mathbf{r}_{ij}\|^3}\right)\\ &= -\frac{1}{4\pi\|\mathbf{r}_{ij}\|^3}\left(\mathbf{I}-\frac{3}{\|\mathbf{r}_{ij}\|^2}\mathbf{r}_{ij}\mathbf{r}_{ij}^T\right)\boldsymbol{\mu}_{ij}\\ &= -\boldsymbol{\mathcal{D}}_{ij}\boldsymbol{\mu}_{ij}\end{aligned} \tag{25}$$

where $\mathbf{I}$ is the identity matrix, and $\boldsymbol{\mathcal{D}}_{ij}$ is called the point-function demagnetizing tensor [Moskowitz and Della Torre 1966]. $\boldsymbol{\mathcal{D}}_{ij}$ is a function of $\mathbf{r}_{ij}$. Because $\mathbf{r}_{ij}$ remains constant for all iterations in a rigid-body simulation step, we pre-compute $\boldsymbol{\mathcal{D}}_{ij}$ and use it for each iteration.

Shown in Algorithm 1 is the pseudocode of magnetic simulation. In each step, we calculate $\mathbf{H}_{\text{eff}}$ for each magnetic moment, $\mathbf{m}$, and update the rotation of $\mathbf{m}$ using Equation (12). For each $\mathbf{m}$, the error is defined to be $\|\mathbf{m}\times\mathbf{h}\|$, where $\mathbf{h}$ represents the normalized $\mathbf{H}_{\text{eff}}$. The iterations continue until either the error sum falls below the pre-defined threshold ϵ or the number of iterations reaches the pre-defined upper limit. In most cases, the magnetic equilibrium is reached with fewer than 30 iterations.

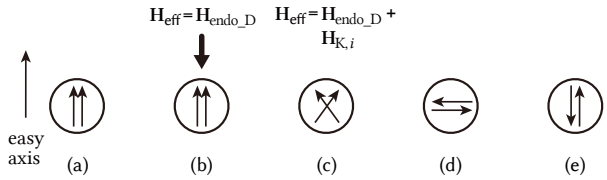

Fig. 10. Magnetization dynamics for remanence.

For each step of rigid-body simulation, the magnetic simulator presented in Algorithm 1 is first run to determine the per-cell magnetic moments. Using them, the magnetic force and torque are calculated in the way Appendix A describes, and then the rigid-body solver is invoked.

4.6 Magnetic Remanence

Magnetic remanence refers to the tendency of preserving magnetization, $\mathbf{M}$, for a certain period of time. A soft ferromagnet with remanence behaves as if it were a permanent magnet. Recall that the magnetization of a permanent magnet is aligned with an easy axis. The necessary condition for a soft ferromagnet to have remanence is that its current magnetization, $\mathbf{M}$, should be (nearly) aligned with an easy axis, as illustrated in Fig. 10-(a).

When $\mathbf{m}_1$ and $\mathbf{m}_2$ are aligned with an easy axis, $\mathbf{H}_{\text{K},1}$ and $\mathbf{H}_{\text{K},2}$ (defined in Equation (24)) become zero, as discussed in Section 3.3. Consequently, $\mathbf{H}_{\text{eff}} = \mathbf{H}_{\text{A}} + \mathbf{H}_{\text{endo\_D}}$ for each magnetic moment in Fig. 10-(a). Note that $\mathbf{H}_{\text{endo\_D}}$ and the current magnetization $\mathbf{M}$ have the opposite directions (Equation (23)).

Suppose that $\mathbf{H}_{\text{A}} = \mathbf{0}$. Then, $\mathbf{H}_{\text{eff}}$ becomes identical to $\mathbf{H}_{\text{endo\_D}}$, as shown in Fig. 10-(b), and $\mathbf{m}_1$ and $\mathbf{m}_2$ will be rotated toward the direction of $\mathbf{H}_{\text{endo\_D}}$. Consequently, $\mathbf{m}_1$ and $\mathbf{m}_2$ are not aligned with the easy axis any longer, as shown in Fig. 10-(c). Then, $\mathbf{H}_{\text{K},i}$ revives and again drives each magnetic moment to be aligned with the easy axis.

$\mathbf{H}_{\text{endo\_D}}$ and $\mathbf{H}_{\text{K},i}$ battle with each other. If neither of them is dominant, we may be in quasi-equilibrium, where $\mathbf{M}$ is neither saturated nor decreased continuously, i.e., $\mathbf{M}$ is preserved for a while. This represents weak remanence. If $\mathbf{H}_{\text{K},i}$ is dominant, however, $\mathbf{m}_1$ and $\mathbf{m}_2$ will be aligned with the easy axis such that $\mathbf{M}$ will be saturated. This represents strong remanence.

It is interesting to look into the case where $\mathbf{H}_{\text{endo\_D}}$ is dominant, decreasing $\mathbf{M}$ to zero, as illustrated in Fig. 10-(d). Because $\mathbf{M}$ is zero, so is $\mathbf{H}_{\text{endo\_D}}$. Consequently $\mathbf{H}_{\text{eff}} = \mathbf{H}_{\text{K},i}$. Note that, according to Equation (24), $\mathbf{H}_{\text{K},1}$ and $\mathbf{H}_{\text{K},2}$ will have the same magnitude and opposite directions. Therefore, $\mathbf{m}_1$ and $\mathbf{m}_2$ will be kept being opposite while making the spiral motions presented in Fig. 3. Eventually, they will be aligned with the easy axis, as shown in Fig. 10-(e), one in the same direction and the other in the opposite direction, keeping $\mathbf{M}$ zero.

For a step in the rigid-body simulation, $\mathbf{m}_1$ and $\mathbf{m}_2$ computed in the previous step are taken and updated. Obviously, remanence would not be implemented without utilizing this temporal coherence.

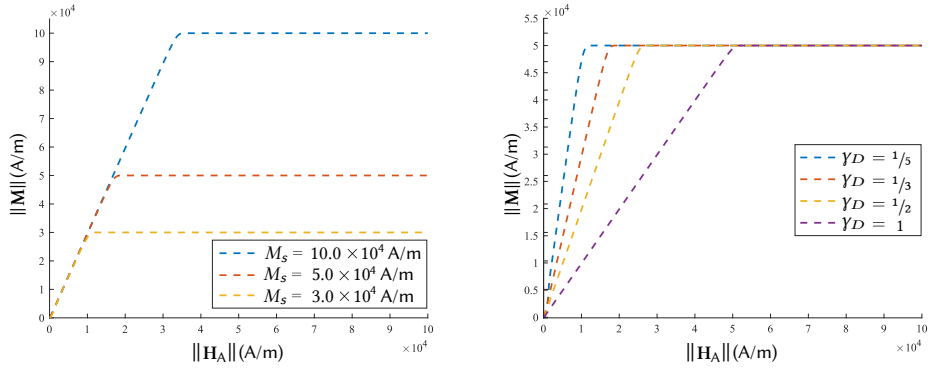

(a) $\gamma_D = 1/3$ (b) $M_s = 5.0 \times 10^4$ A/m

Fig. 11. Relation between $\mathbf{M}$ and $\mathbf{H}_A$ for a single-cell soft ferromagnet: (a) Three materials, each with different M_s, share the same γ_D. It determines the slope of the curve when $\|\mathbf{H}_A\| < H_s$. (b) Four materials, each with different γ_D, share the same M_s.

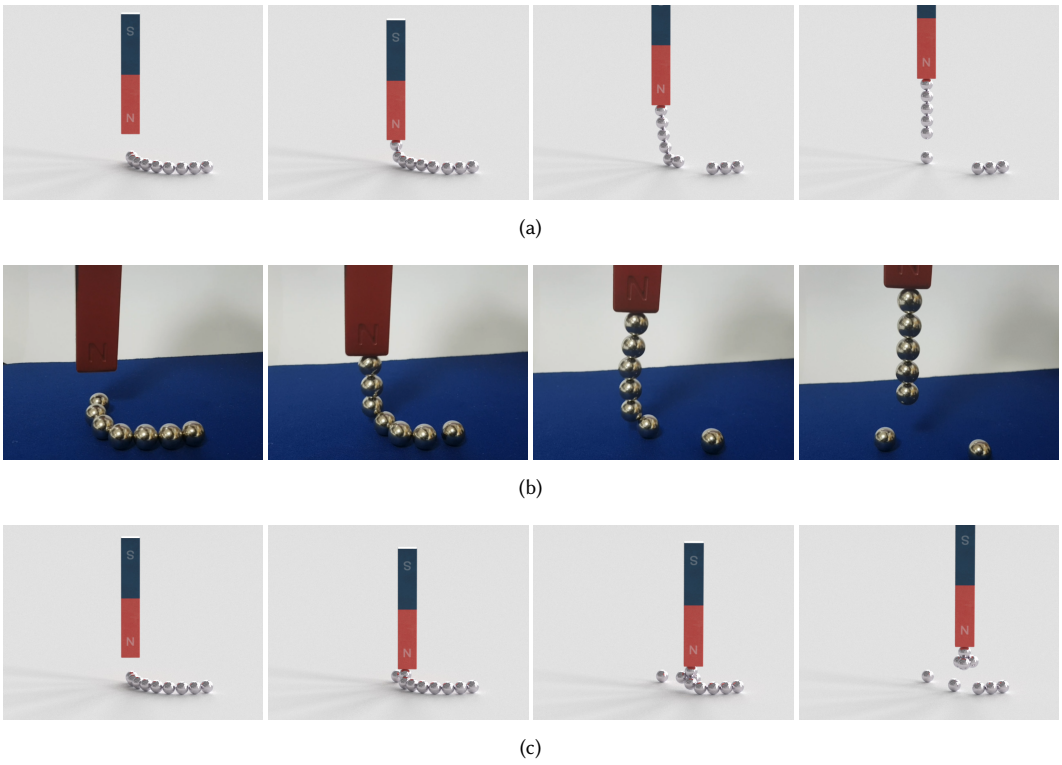

(a)

(b)

(c)

Fig. 12. Mutual induction: (a) Simulation with mutual induction. (b) Real-world experiment. (c) Simulation without mutual induction.

5 EXPERIMENTAL RESULTS AND DISCUSSIONS

5.1 Validation of Magnetization Curve

In order to prove that our magnet modeling and simulation are in accord with Equation (21), we conducted an experiment under the same environment presented in Section 4.4, i.e., we used a single-cell object exposed to only $\mathbf{H}_E$ and assigned two magnetic moments to the cell. Fig. 11 shows the simulation results. They coincide with the theoretical values.

5.2 Mutual Induction

In Fig. 12-(a), only a single ball is initially lifted toward the magnet. The second ball is induced by that lifted ball as well as the bar magnet, eventually resulting in a chain of induced magnets. Fig. 12-(b) shows the same phenomenon captured in a real-world experiment. Fig. 12-(c) shows the result obtained by disabling mutual induction. As each ball is induced only by the bar magnet, fewer balls are lifted toward the bar magnet.

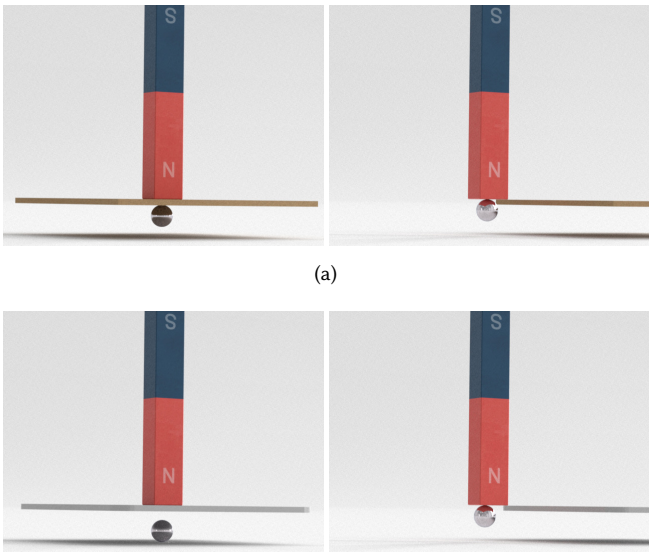

Fig. 13. Magnetic shielding: (a) Wood plate. (b) Iron plate.

Mutual induction makes it possible to conduct numerous magnetic experiments in the virtual world. Fig. 13 shows an experiment popularly made in science classes. A plate is inserted between a bar magnet and an iron ball. If the plate is made of a non-magnetic material such as wood and glass, it does not affect the magnetic interaction between the bar magnet and the ball. Fig. 13-(a) shows that the ball is lifted toward the bar magnet regardless of the existence of the wood plate.

In contrast, if an iron plate is inserted, for example, it is induced by the bar magnet to generate its own magnetic field, which significantly offsets the magnetic field generated by the bar magnet.

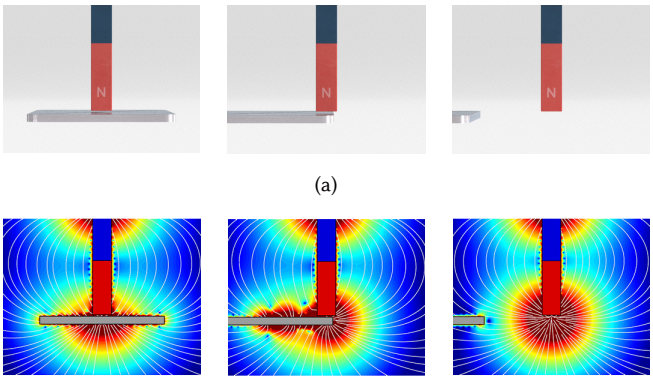

Fig. 14. Visualization of magnetic field lines and force magnitudes: (a) Magnetic shielding with iron plate. (b) The magnetic field lines are in gray and the magnetic forces' magnitudes are in rainbow colors, **VIBGYOR**, where **V**iolet is the weakest and **R**ed is the strongest.

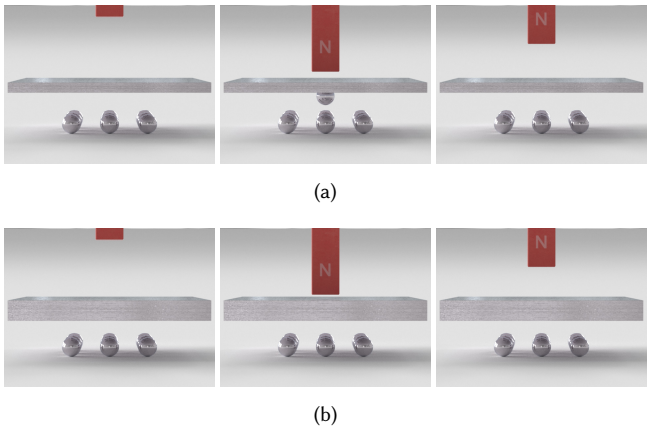

Fig. 15. Different shielding objects: (a) A thin iron plate. (b) A thick plate.

Consequently, the iron ball is weakly induced and may not be lifted toward the bar magnet. This is often called *magnetic shielding*. See the left of Fig. 13-(b). As soon as we remove the plate, however, the ball is lifted toward the magnet, as shown on the right of Fig. 13-(b). Fig. 14 visualizes the magnetic field lines and the magnitudes of forces for the example of magnetic shielding with an iron plate. Observe that the iron plate weakens the magnetic forces in the area under the bar magnet.

The shielding effect increases proportionately to the volume of the shielding object. In Fig. 15-(a), the iron plate is thin and the magnetic field generated by it is weak. A single ball is strongly induced and lifted toward the bar magnet. The other balls are weakly induced. In contrast, the magnetic field generated by the thick iron plate in Fig. 15-(b) is strong, and no ball is lifted.

5.3 Magnetic Remanence

Fig. 16-(a) shows a permanent magnet (bar magnet) and two kinds of soft ferromagnets, a nail and three iron balls, which are not induced yet. In Fig. 16-(b), the nail is in contact with the bar magnet and induced. Fig. 16-(c) and -(d) show that the iron balls are induced by the remanence of the nail.

In Fig. 17-(a) and -(b), a large number of iron balls are lifted toward the crane magnet, and a heap of induced magnets is formed due to mutual induction. In Fig. 17-(c), we reduce the magnetization of the crane magnet, and many of the induced magnets fall down to the ground because the gravitational force exceeds the magnetic forces exerted on them. In Fig. 17-(d), the crane magnet becomes completely unmagnetized, but a few induced balls still hang from the crane magnet due to remanence.

5.4 Performance

We made all experiments with Intel Core i7-4770 3.40 GHz CPU, 20 GB memory, and Nvidia GeForce GTX 780. The magnetic simulation was implemented in CUDA, and the rigid-body simulation was built upon the open-source library, Bullet Physics [Coumans 2015]. All scenes were rendered with Mitsuba [Jakob 2010].

The performances of the experiments presented so far are listed in Table 1. Δt represents the time step size in the rigid-body simulation,

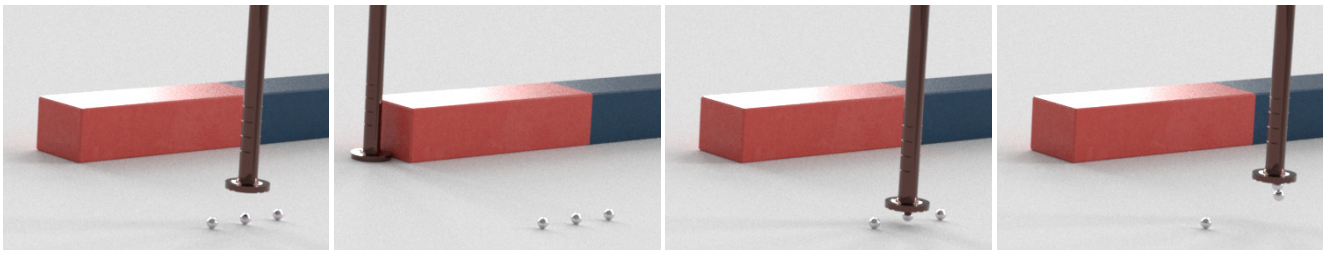

(a) (b) (c) (d)

Fig. 16. Remanence simulation.

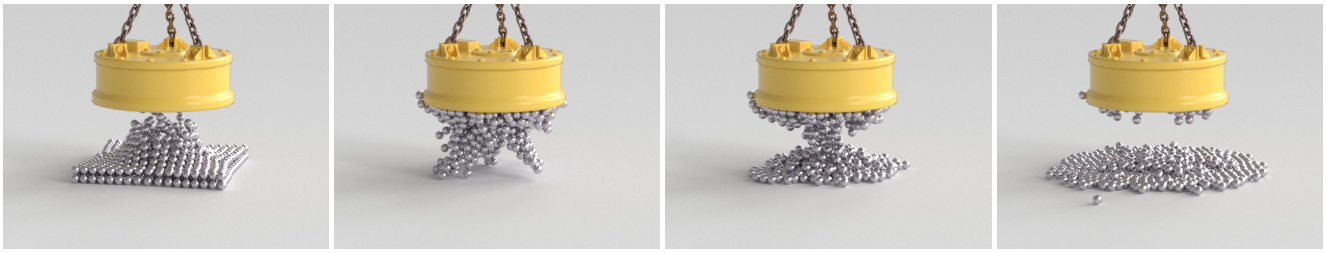

(a) (b) (c) (d)

Fig. 17. The crane magnet and a large number of soft ferromagnets.

Table 1. Performance data: Δt, T_m, and T_r are all in milliseconds.

Scene	# of cells	Δt	T_m	T_r
ball chain (Fig. 12)	28	4	2.5	1.3
wood plate (Fig. 13-(a))	32	10	2.4	1.0
iron plate (Fig. 13-(b))	191	10	8.1	1.1
thin iron (Fig. 15-(a))	140	4	24	4.4
thick iron (Fig. 15-(b))	140	4	24	4.5
nail and balls (Fig. 16)	88	5	1.4	1.4
crane magnet (Fig. 17)	690	1	118	57

T_m is the elapsed time on the magnetic simulation, and T_r is that on the rigid-body simulation.

A problem can be found in our integrated simulation framework. The rigid-body simulator requires the magnetic forces and torques at time t to compute the velocities and poses at $t + \Delta t$. The magnetic forces and torques are computed using the magnetic moments, which are provided by the magnetic simulator presented in Algorithm 1. Taking the magnetic moments at t as input, the magnetic simulator updates them with the time step size δt. Consequently, the rigid-body simulator uses the magnetic forces and torques at $t + \delta t \times iter$, where $iter$ denotes the iteration count in Algorithm 1. Fortunately, this discrepancy is negligible because δt is in the order of nanoseconds (whereas Δt is in between 1ms and 10ms in the current implementation) and $iter$ is usually smaller than 30 in our experiments.

5.5 Simulation Stability

When the external field, $\mathbf{H}_\mathrm{E}$, remains constant, the micromagnetic free energy, also known as the magnetic energy, is determined by the magnetization distribution [d'Aquino 2005]. The magnetization dynamics defined by the LLG equation has the so-called *Lyapunov structure* with respect to the micromagnetic free energy, which guarantees that the free energy does not diverge [Podio-Guidugli 2001]. Let G denote the free energy per volume at a point. Then, its change over time is defined as follows:

$$\frac{dG}{dt} = -\mu_0 \eta \left\| \frac{\partial \mathbf{M}}{\partial t} \right\|^2 \leq 0 \tag{26}$$

where μ_0 represents the permeability of the free space and η is the material-specific damping constant. Appendix B proves that the non-divergence of the free energy, presented as an inequality in Equation (26), holds in our numerical simulation.

Even though the Lyapunov structure does not ensure the convergence of the free energy, its tendency to change the free energy toward stable equilibrium points is proven [Podio-Guidugli 2001]. Unfortunately, this tendency might be impeded by numerical errors, and our magnetic simulation is not guaranteed to terminate. In the current implementation, we handle this using the iteration limit presented in Section 4.5.

The magnetization curve in Fig. 6 asserts that $\mathbf{M} = \mathbf{0}$ if $\mathbf{H}_\mathrm{A} = \mathbf{0}$. Appendix C proves that the net magnetic moment of a cell converges

toward zero when $\mathbf{H}_{\mathrm{A}} = \mathbf{0}$ in our simulation, i.e.,

$$\left\| \sum_{k=1}^{n} \mathbf{m}_k^{i+1} \right\|^2 - \left\| \sum_{k=1}^{n} \mathbf{m}_k^{i} \right\|^2 \leq 0 \tag{27}$$

where $\mathbf{m}_k$ denotes the k-th among n magnetic moments.

5.6 Limitations and Future Work

In the experiments presented so far, we used the iron balls for induced magnets since they are popular in real-world experiments and their rigid-body simulation is largely stable. When a non-spherical object is rotated by a torque generated by magnetic forces, it may easily penetrate other objects, leading to an unstable simulation. Fortunately, the saturated magnetization helps prevent the torque from becoming excessively large. However, we are not completely free from the instability problem. When the centers of two cells coincide, for example, the magnetic force and torque may go to infinity. Our future work includes investigating robust magnetic interaction for rigid-body simulation [De Graef and Beleggia 2009].

We used spherical cells mainly because the analytic solution of $\mathbf{H}_{\mathrm{endo\_D}}$ is available (Equation (16)). Given an object with an arbitrary geometry such as sharp corners, the cell resolution needs to be increased for quasi-uniform distribution. This often degrades efficiency. Our future work may include discretizing with arbitrarily-shaped cells and computing $\mathbf{H}_{\mathrm{endo\_D}}$ for each cell using [Beleggia and De Graef 2005].

In order to port the micro-scale magnetization dynamics into the macro scale, we replace a huge number of infinitesimal magnetic moments with a small number of large magnetic moments which are stored in cells. Even though simulation at the macro scale produces satisfactory results, we lose one of the important properties of magnetics, which is the *exchange anisotropy* [Aharoni 2000]. We will investigate how to integrate the exchange anisotropy into our simulation framework.

It is possible to control convergence speed in magnetization by adjusting α in Equation (9). In the current implementation, however, we used the same α for all magnetic objects. We envision that a variety of magnetization dynamics could be created with varying α. In principle, the demagnetizing factor, γ_D, is related to the shape of a magnetic cell. However, it can be adjusted regardless of the shape to define the susceptibility of, for example, a paramagnet. Moreover, if η in Equation (4) is negative, the magnetization of an induced magnet will be damped reversely, making it antiparallel to the effective magnetic field. Then, it would act like a diamagnet or a superconductor. These experiments are left as future works.

Magnetic interactions are fundamentally generated by electric interactions. However, our method does not take this into account. In the future, it would be necessary to carry out research on those electrical properties.

6 CONCLUSION

We presented a novel method of implementing magnetization dynamics. We decompose each magnetic object into uniform cells and assign multiple magnetic moments to a cell. The temporal change of the magnetic moments is simulated using the Landau-Lifshitz-Gilbert equation. Our method not only adjusts each cell's magnetization exposed to the effective magnetic field but also limits its upper bound so as to prevent the magnetic force and torque from becoming excessively large. It enables stable rigid-body simulation of magnetic objects. The method also facilitates implementing magnetic mutual induction and remanence.

In addition to animations and visual effects, our work can be used for virtual magnet experiments. A major topic in elementary-school science classes is on magnets, and many efforts have been made to conduct magnet experiments in the virtual world. Over the past few years, a new wave of interest in virtual reality has formed. It makes the virtual magnet experiments a more feasible goal especially because the cost barrier of manipulating virtual objects in a realistic way has been dramatically reduced. Our work enables various magnet experiments to be conducted in the virtual world.

ACKNOWLEDGMENTS

This work was supported by the National Research Foundation of Korea (NRF) Grant funded by the Korea government (No. NRF-2016R1A2B3014319 and NRF-2017M3C4A7066316).

REFERENCES

JJ Abbott, O Ergeneman, MP Kummer, AM Hirt, and BJ Nelson. 2007. Modeling magnetic torque and force for controlled manipulation of soft-magnetic bodies. *IEEE Transactions on Robotics* 23, 6 (2007), 1247–1252.

A Aharoni. 2000. *Introduction to the Theory of Ferromagnetism*. Vol. 109. Clarendon Press.

S Bachthaler, F Sadlo, R Weeber, S Kantorovich, C Holm, and D Weiskopf. 2012. Magnetic flux topology of 2D point dipoles. In *Computer Graphics Forum*, Vol. 31. Wiley Online Library, 955–964.

M Beleggia and M De Graef. 2005. General magnetostatic shape–shape interactions. *Journal of Magnetism and Magnetic Materials* 285, 1-2 (2005), L1–L10.

W Brown. 1979. Thermal fluctuation of fine ferromagnetic particles. *IEEE Transactions on Magnetics* 15, 5 (1979), 1196–1208.

Q Cao, X Han, and L Li. 2014. Configurations and control of magnetic fields for manipulating magnetic particles in microfluidic applications: magnet systems and manipulation mechanisms. *Lab on a Chip* 14, 15 (2014), 2762–2777.

E Coumans. 2015. Bullet physics simulation. In *ACM SIGGRAPH 2015 Courses*. ACM, 7.

M d'Aquino. 2005. *Nonlinear magnetization dynamics in thin-films and nanoparticles*. Ph.D. Dissertation. Università degli Studi di Napoli Federico II.

M De Graef and M Beleggia. 2009. General magnetostatic shape–shape interaction forces and torques. *Journal of Magnetism and Magnetic Materials* 321, 15 (2009), L45–L51.

M d'Aquino, C Serpico, and G Miano. 2005. Geometrical integration of Landau–Lifshitz–Gilbert equation based on the mid-point rule. *J. Comput. Phys.* 209, 2 (2005), 730–753.

TL Gilbert. 1955. A Lagrangian formulation of the gyromagnetic equation of the magnetization field. *Phys. Rev.* 100 (1955), 1243.

R Grössinger. 1981. A critical examination of the law of approach to saturation. I. Fit procedure. *physica status solidi (a)* 66, 2 (1981), 665–674.

GF Herrmann. 1963. Resonance and high frequency susceptibility in canted antiferromagnetic substances. *Journal of Physics and Chemistry of Solids* 24, 5 (1963), 597–606.

T Ishikawa, Y Yue, K Iwasaki, Y Dobashi, and T Nishita. 2013. Visual Simulation of Magnetic Fluid Using a Procedural Approach for Spikes Shape. In *Computer Vision, Imaging and Computer Graphics. Theory and Application*. Springer, 112–126.

JD Jackson. 1999. Classical electrodynamics. *American Journal of Physics* 67, 9 (1999), 841–842.

W Jakob. 2010. Mitsuba renderer. (2010). http://www.mitsuba-renderer.org.

R Khymyn, I Lisenkov, V Tiberkevich, BA Ivanov, and A Slavin. 2017. Antiferromagnetic THz-frequency Josephson-like Oscillator Driven by Spin Current. *Scientific Reports* 7 (2017), 43705.

T Klein and T Ertl. 2004. Illustrating Magnetic Field Lines using a Discrete Particle Model.. In *VMV*, Vol. 4. 387–394.

M Kruzík and A Prohl. 2006. Recent developments in the modeling, analysis, and numerics of ferromagnetism. *SIAM review* 48, 3 (2006), 439–483.

M Lakshmanan. 2011. The fascinating world of the Landau–Lifshitz–Gilbert equation: an overview. *Philosophical Transactions of the Royal Society of London A: Mathematical, Physical and Engineering Sciences* 369, 1939 (2011), 1280–1300.
R Moskowitz and E Della Torre. 1966. Theoretical aspects of demagnetization tensors. *IEEE Transactions on Magnetics* 2, 4 (1966), 739–744.
M Müller, D Charypar, and M Gross. 2003. Particle-based fluid simulation for interactive applications. In *Proceedings of the 2003 ACM SIGGRAPH/Eurographics symposium on Computer animation*. Eurographics Association, 154–159.
Y Nakatani, Y Uesaka, and N Hayashi. 1989. Direct solution of the Landau-Lifshitz-Gilbert equation for micromagnetics. *Japanese Journal of Applied Physics* 28, 12R (1989), 2485.
JA Osborn. 1945. Demagnetizing factors of the general ellipsoid. *Physical review* 67, 11-12 (1945), 351.
J Park, K Lee, and J Han. 2016. Interactive visualization of magnetic field for virtual science experiments. *Journal of Visualization* 19, 1 (2016), 129–139.
P Podio-Guidugli. 2001. On dissipation mechanisms in micromagnetics. *The European Physical Journal B-Condensed Matter and Complex Systems* 19, 3 (2001), 417–424.
C Serpico, ID Mayergoyz, and G Bertotti. 2001. Numerical technique for integration of the Landau–Lifshitz equation. *Journal of Applied Physics* 89, 11 (2001), 6991–6993.
B Thomaszewski, A Gumann, S Pabst, and W Strasser. 2008. Magnets in Motion. In *ACM SIGGRAPH Asia 2008 Papers (SIGGRAPH Asia '08)*. ACM, New York, NY, USA, Article 162, 9 pages. DOI: http://dx.doi.org/10.1145/1457515.1409115
W Yoon, N Lee, K Um, and J Han. 2014. Computer-generated iron filing art. *The Visual Computer* 30, 6-8 (2014), 889–895.

APPENDIX A MAGNETIC FORCES AND TORQUES

The magnetic force (**F**) and torque (**T**) exerted on a magnetic moment ($\boldsymbol{\mu}$) are determined by the applied magnetic field ($\mathbf{H}_\mathrm{A}$). According to Ampere's law, **F** and **T** can be formulated in a form of a Taylor series expansion. The leading terms of the expansion can be phrased as follows:

$$\mathbf{F} = \mu_0 \nabla(\boldsymbol{\mu} \cdot \mathbf{H}_\mathrm{A}) \tag{28}$$

$$\mathbf{T} = \mu_0 \boldsymbol{\mu} \times \mathbf{H}_\mathrm{A} \tag{29}$$

where μ_0 represents the permeability of the free space. When the external magnetic field is ignored, Equations (28) and (29) can be rephrased using Equation (15) to be exclusively expressed with the magnetic moment and the other magnetic moments:

$$\mathbf{F} = \frac{\mu_0}{4\pi} \sum_i \sum_j \left[\frac{-15\mathbf{r}_{ij}\Big((\boldsymbol{\mu} \cdot \mathbf{r}_{ij}) \cdot (\boldsymbol{\mu}_{ij} \cdot \mathbf{r}_{ij})\Big)}{\|\mathbf{r}_{ij}\|^7} + \frac{3\mathbf{r}_{ij}(\boldsymbol{\mu} \cdot \boldsymbol{\mu}_{ij}) + 3\Big(\boldsymbol{\mu}(\boldsymbol{\mu}_{ij} \cdot \mathbf{r}_{ij}) + \boldsymbol{\mu}_{ij}(\boldsymbol{\mu} \cdot \mathbf{r}_{ij})\Big)}{\|\mathbf{r}_{ij}\|^4} \right] \tag{30}$$

$$\mathbf{T} = \frac{\mu_0}{4\pi} \sum_i \sum_j \left[\frac{3\left(\boldsymbol{\mu} \times \mathbf{r}_{ij}\right)\left(\boldsymbol{\mu}_{ij} \times \mathbf{r}_{ij}\right)}{\|\mathbf{r}_{ij}\|^5} - \frac{\boldsymbol{\mu} \times \boldsymbol{\mu}_{ij}}{\|\mathbf{r}_{ij}\|^3} \right] \tag{31}$$

where $\boldsymbol{\mu}_{ij}$ is the magnetic moment of cell C_{ij}, and $\mathbf{r}_{ij}$ is the vector from the center of C_{ij} to the position of $\boldsymbol{\mu}$. See [Thomaszewski et al. 2008] for more detail.

APPENDIX B NON-DIVERGENCE OF MAGNETIZATION DYNAMICS WITH MIDPOINT INTEGRATION

As presented in [d'Aquino et al. 2005], $\mathbf{H}_\mathrm{eff}$ can be expressed in terms of the magnetization derivative of the free energy:

$$\mathbf{H}_\mathrm{eff} = -\frac{\partial G}{\partial \mathbf{M}} \tag{32}$$

In our numerical scheme, Equation (32) can be modified with the first-order approximations of G and **M** according to Equation (11):

$$\left(G^{i+1} - G^i\right) = -M_s\left(\mathbf{m}^{i+1} - \mathbf{m}^i\right) \cdot \mathbf{H}_\mathrm{eff}^{i+\frac{1}{2}} \tag{33}$$

Let us dot-multiply both sides of Equation (12) by $-M_s\mathbf{H}_\mathrm{eff}^{i+\frac{1}{2}}$:

$$-M_s\left(\mathbf{m}^{i+1} - \mathbf{m}^i\right) \cdot \mathbf{H}_\mathrm{eff}^{i+\frac{1}{2}} = \frac{\gamma \Delta t M_s}{2\left(1+\alpha^2\right)} \left(\left(\mathbf{m}^{i+1} + \mathbf{m}^i\right) \times \boldsymbol{\mathcal{H}}^{i+\frac{1}{2}} \right) \cdot \mathbf{H}_\mathrm{eff}^{i+\frac{1}{2}} \tag{34}$$

The left-hand side of Equation (34) can be replaced by $G^{i+1} - G^i$ according to Equation (33). Therefore, Equation (34) can be modified as follows:

$$G^{i+1} - G^i = \frac{\gamma \Delta t M_s}{2\left(1+\alpha^2\right)} \left(\left(\mathbf{m}^{i+1} + \mathbf{m}^i\right) \times \boldsymbol{\mathcal{H}}^{i+\frac{1}{2}} \right) \cdot \mathbf{H}_\mathrm{eff}^{i+\frac{1}{2}} \tag{35}$$

Using Equations (9) and (12), the right-hand side of Equation (35) is rephrased as follows:

$$\begin{aligned} & G^{i+1} - G^i \\ &= \frac{\gamma \Delta t M_s}{\left(1+\alpha^2\right)} \left(\mathbf{m}^{i+\frac{1}{2}} \times \left(\mathbf{H}_\mathrm{eff}^{i+\frac{1}{2}} + \alpha \mathbf{m}^{i+\frac{1}{2}} \times \mathbf{H}_\mathrm{eff}^{i+\frac{1}{2}} \right) \right) \cdot \mathbf{H}_\mathrm{eff}^{i+\frac{1}{2}} \\ &= \frac{\gamma \Delta t M_s \alpha}{\left(1+\alpha^2\right)} \left(\mathbf{m}^{i+\frac{1}{2}} \times \left(\mathbf{m}^{i+\frac{1}{2}} \times \mathbf{H}_\mathrm{eff}^{i+\frac{1}{2}} \right) \right) \cdot \mathbf{H}_\mathrm{eff}^{i+\frac{1}{2}} \\ &\leq 0 \end{aligned} \tag{36}$$

This shows that the free energy does not diverge.

APPENDIX C CONVERGENCE OF NET MAGNETIZATION OF MULTIPLE MAGNETIC MOMENTS

Given n magnetic moments in a cell, let us denote the k-th as $\mathbf{m}_k$. Assuming that $\mathbf{H}_\mathrm{eff} = \mathbf{H}_\mathrm{endo\_D}$, Equations (8), (18), and (23) lead to the following:

$$\frac{d\mathbf{m}_k}{dt} = \frac{\gamma\gamma_D M_s}{n\left(1+\alpha^2\right)} \left(\mathbf{m}_k \times \sum_{i=1}^n \mathbf{m}_i + \alpha \mathbf{m}_k \times \left(\mathbf{m}_k \times \sum_{i=1}^n \mathbf{m}_i \right) \right) \tag{37}$$

The sum of $\frac{d\mathbf{m}_k}{dt}$ (for $k = 1, 2, \ldots, n$) is calculated as follows:

$$\begin{aligned} & \sum_{k=1}^n \frac{d\mathbf{m}_k}{dt} \\ &= \frac{\gamma\gamma_D M_s}{n\left(1+\alpha^2\right)} \left(\sum_{k=1}^n \mathbf{m}_k \times \sum_{i=1}^n \mathbf{m}_i + \alpha \sum_{k=1}^n \left(\mathbf{m}_k \times \left(\mathbf{m}_k \times \sum_{i=1}^n \mathbf{m}_i \right) \right) \right) \\ &= \frac{\gamma\gamma_D M_s \alpha}{n\left(1+\alpha^2\right)} \sum_{k=1}^n \left(\mathbf{m}_k \times \left(\mathbf{m}_k \times \sum_{i=1}^n \mathbf{m}_i \right) \right) \end{aligned} \tag{38}$$

Note that $\sum_{k=1}^n \mathbf{m}_k$ equals $\sum_{i=1}^n \mathbf{m}_i$. Using the vector identity, $\mathbf{a} \times (\mathbf{b} \times \mathbf{c}) = (\mathbf{a} \cdot \mathbf{c})\,\mathbf{b} - (\mathbf{a} \cdot \mathbf{b})\,\mathbf{c}$, Equation (38) is rephrased as follows:

$$\sum_{k=1}^n \frac{d\mathbf{m}_k}{dt} = \frac{\gamma\gamma_D M_s \alpha}{\left(1+\alpha^2\right)} \left(\frac{1}{n} \sum_{k=1}^n \left(\mathbf{m}_k \cdot \sum_{i=1}^n \mathbf{m}_i \right) \mathbf{m}_k - \sum_{i=1}^n \mathbf{m}_i \right) \tag{39}$$

Consider the dot product of Equation (39) and $\sum_{k=1}^{n} \mathbf{m}_k$:

$$\begin{aligned}
&\sum_{k=1}^{n} \mathbf{m}_k \cdot \sum_{k=1}^{n} \frac{d\mathbf{m}_k}{dt} \\
&= \frac{\gamma\gamma_D M_s \alpha}{(1+\alpha^2)} \left(\frac{1}{n} \sum_{k=1}^{n} \left(\mathbf{m}_k \cdot \sum_{i=1}^{n} \mathbf{m}_i \right) \mathbf{m}_k \cdot \sum_{k=1}^{n} \mathbf{m}_k - \sum_{i=1}^{n} \mathbf{m}_i \cdot \sum_{k=1}^{n} \mathbf{m}_k \right) \\
&= \frac{\gamma\gamma_D M_s \alpha}{(1+\alpha^2)} \left(\frac{1}{n} \sum_{k=1}^{n} \left\| \mathbf{m}_k \cdot \sum_{i=1}^{n} \mathbf{m}_i \right\|^2 - \left\| \sum_{i=1}^{n} \mathbf{m}_i \right\|^2 \right) \qquad (40)
\end{aligned}$$

Since $\|\mathbf{m}_k\| = 1$, Equation (40) is always less than or equal to zero:

$$\left\| \mathbf{m}_k \cdot \sum_{i=1}^{n} \mathbf{m}_i \right\|^2 \leq \left\| \sum_{i=1}^{n} \mathbf{m}_i \right\|^2 \qquad (41)$$

$$\frac{1}{n} \sum_{k=1}^{n} \left\| \mathbf{m}_k \cdot \sum_{i=1}^{n} \mathbf{m}_i \right\|^2 \leq \left\| \sum_{i=1}^{n} \mathbf{m}_i \right\|^2 \qquad (42)$$

Now consider Equation (27). It can be rephrased as follows:

$$\left(\sum_{k}^{n} \mathbf{m}_k^{i+1} + \sum_{k}^{n} \mathbf{m}_k^{i} \right) \cdot \left(\sum_{k}^{n} \mathbf{m}_k^{i+1} - \sum_{k}^{n} \mathbf{m}_k^{i} \right) \leq 0. \qquad (43)$$

Equations (10) and (11) turn Equation (43) into:

$$\sum_{k}^{n} \mathbf{m}_k^{i+\frac{1}{2}} \cdot \sum_{k}^{n} \left(\frac{d\mathbf{m}_k}{dt} \right)^{i+\frac{1}{2}} \leq 0 \qquad (44)$$

The left side is in fact identical to Equation (40). Therefore, Equation (44) is always true. Let $\mathbf{c}$ denote $\lim_{i\to\infty} \sum_{k}^{n} \mathbf{m}_k^i$. Note that $\lim_{i\to\infty} \sum_{k}^{n} \left(\frac{d\mathbf{m}_k}{dt} \right)^{i+\frac{1}{2}}$ should be zero. Then, taking the limit of both sides of Equation (40), we obtain the following:

$$\frac{1}{n} \sum_{k=1}^{n} \left\| \lim_{i\to\infty} \mathbf{m}_k^i \cdot \mathbf{c} \right\|^2 - \|\mathbf{c}\|^2 = 0 \qquad (45)$$

This holds only when $\lim_{i\to\infty} \mathbf{m}_k^i = \mathbf{c}$ for $k = 1, 2, \ldots, n$ or $\mathbf{c} = \mathbf{0}$. The first case may not happen, and therefore $\mathbf{c} = \mathbf{0}$.